https://doi.org/10.3311/PPee.41626

Periodica Polytechnica Electrical Engineering and Computer Science

Model-free Predictive Current Control Combined with Sliding Mode Voltage Control for Wind Power Grid-connected System

Tailong Xiong[1*], Shihong Gan[1]

[1] Department of Electrical Automation, Logistics Engineering College, Shanghai Maritime University, 1550 Haigang Avenue, Pudong New Area, 201306 Shanghai, China
[*] Corresponding author, e-mail: gig216@163.com

Received: 16 July 2025, Accepted: 04 December 2025, Published online: 18 December 2025

Abstract

In the context of global energy transition towards low-carbonization, direct-drive permanent magnet synchronous wind power generation systems have become one of the mainstream power generation equipment due to their unique advantages. However, traditional control algorithms are difficult to cope with the complex operating conditions of the grid-side converter. This paper aims to improve the grid connection control algorithm of the direct-drive wind power system. It proposes a collaborative algorithm based on sliding mode control (SMC) for DC link voltage control and model-free predictive control (MFPC) for current control. Additionally, a discrete extended state observer (DESO) is designed to observe the unknown state variables in the system to avoid the influence of model mismatch. By comparing the simulation results of different algorithms of the control system under internal and external disturbances, it is verified that the proposed algorithm can more effectively track the *d-q* axis target current and stabilize the DC link voltage. The proposed method can help wind turbine generators operate efficiently in harsh environments, and has certain theoretical and engineering value for improving the grid connection performance of direct-drive wind power and promoting the consumption of new energy.

Keywords

wind power grid connection, sliding mode control, model-free predictive current control, robustness against parameter perturbation

1 Introduction

Against the backdrop of the global energy structure accelerating its transition towards low-carbonization, wind power has emerged as one of the core pillars driving the decarbonization of the energy system. The direct-drive permanent magnet synchronous wind power system, as a mainstream equipment in wind power generation, is characterized by low failure rate, high reliability, and high efficiency [1, 2]. The grid-side converter serves as the hub for energy interaction between the wind power generation system and the grid. Its control algorithm directly affects the power transmission stability, power quality, and grid adaptability of the system. In traditional vector control, the proportional-integral (PI) control algorithm has issues such as slow dynamic response and insufficient robustness when dealing with complex working conditions such as grid voltage fluctuations, wind speed changes, and variations in system internal parameters [3, 4]. To solve these issues, advanced control algorithms such as fuzzy control, feedback linearization control, model predictive control and sliding mode control have been applied to the control of wind power generation systems [2, 4–6].

Osman and Alsokhiry [7] proposed a sliding mode control with an improved reaching law for the direct-drive permanent magnet synchronous generator wind energy conversion system. Compared with PI control, it can achieve better control effects on current and DC link voltage. Model predictive control (MPC) technology has demonstrated unique advantages in the field of power converter control by virtue of its multi-constraint processing capability and rolling optimization mechanism [8]. He et al. [4] proposed an MPC algorithm that combines the DC link voltage and power regulation terms into a single cost function, eliminating the traditional cascaded control structure and further reducing the DC link voltage error. Ma et al. [9] proposed an MPC algorithm based on constraints including power, voltage amplitude, and ramping, which enhances the power control performance of wind turbines and their grid support capability.

Cite this article as: Xiong, T., Gan, S. "Model-free Predictive Current Control Combined with Sliding Mode Voltage Control for Wind Power Grid-connected System", Periodica Polytechnica Electrical Engineering and Computer Science, 2025. https://doi.org/10.3311/PPee.41626

However, wind power generation systems are mostly installed in harsh environments, which inevitably causes changes in system parameters. The performance of traditional MPC highly depends on the accuracy of the system mathematical model. When system parameters change or external disturbances occur, the control system may make misjudgments based on a mismatched model and fail to select the optimal control quantity, thereby degrading the dynamic performance and robustness of the control system [10, 11]. To address this, in recent years, scholars have proposed using a model-free predictive control (MFPC) algorithm based on an ultra-local model to solve the impact of parameter variations on the system [12, 13]. MFPC is an improved scheme of MPC. It abandons MPC's dependence on the system model and uses the input and output data of the system for prediction and control, so that it can still maintain good control performance when the model parameters are uncertain or changing [14, 15]. To estimate the unknown state variables in the ultra-local model, methods such as algebraic parameter identification technology [16, 17], extended state observer [18, 19], and sliding mode observer [13, 20] have been proposed by researchers.

This paper focuses on the grid-side connection control of direct-drive wind power generation systems and proposes a collaborative control algorithm (termed SMC-MFPC) that integrates SMC for DC link voltage regulation with MFPC for grid current tracking. This paper designs a DESO to obtain the unknown state variables in the ultra-local model. Simulation experiments are carried out under disturbances including grid voltage dips, wind speed fluctuations, and abrupt changes in filter inductance to validate the effectiveness of the proposed control algorithm and its performance enhancements, ensuring stable and high-quality power transmission to the grid.

2 The model of grid-side converter

In a direct-drive permanent magnet synchronous wind power generation system, the machine-side converter (MSC) converts the wind energy absorbed by the wind turbine into electrical energy, which is transmitted through the DC link to the grid-side converter (GSC) and finally delivered to the power grid. The MSC controls the rotational speed of the wind turbine to reasonably capture wind energy, while the GSC stabilizes the DC link voltage and realizes grid connection. The direct-drive permanent magnet synchronous wind power generation system is shown in Fig. 1, and the current equation of the DC link is:

$$C_{dc}\frac{du_{dc}}{dt} = i_M - i_G . \tag{1}$$

In Eq. (1), C_{dc} is the capacitance of the DC link, and u_{dc} is the DC link voltage.

For the mathematical model of the grid-side three-phase converter in the d-q coordinate system, let f_d and f_q denote

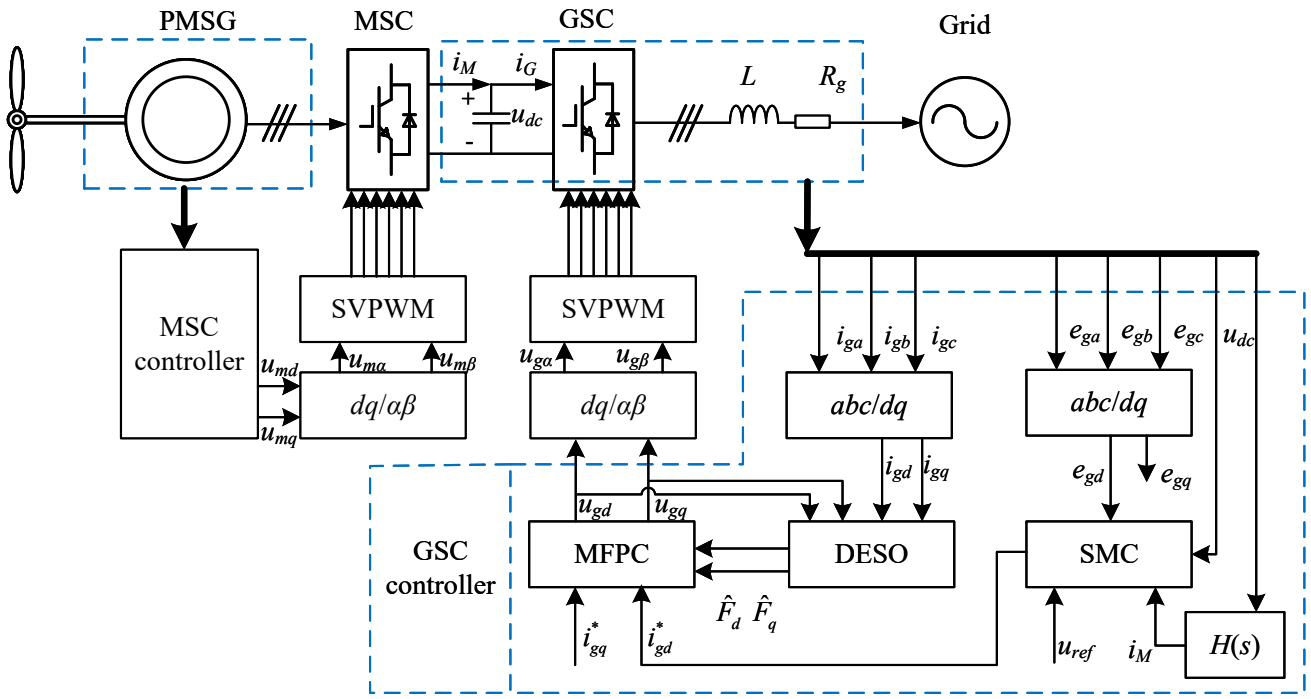

Fig. 1 Control block diagram of wind power system

the lumped disturbances caused by external and internal parameter perturbations of the system, which are finally expressed in the form of an ultra-local model:

$$\begin{cases} \dfrac{di_{gd}}{dt} = \alpha u_{gd} + \left(\dfrac{1}{L} - \alpha\right) u_{gd} - \dfrac{1}{L} R_g i_{gd} + \omega i_{gq} - \dfrac{1}{L} e_{gd} + f_d \\ = \alpha u_{gd} + F_d \\ \dfrac{di_{gq}}{dt} = \alpha u_{gq} + \left(\dfrac{1}{L} - \alpha\right) u_{gq} - \dfrac{1}{L} R_g i_{gq} - \omega i_{gd} - \dfrac{1}{L} e_{gq} + f_q \\ = \alpha u_{gq} + F_q \end{cases}. \tag{2}$$

In Eq. (2), L is the filter inductance, R_g is the filter resistance, e_{gd}, e_{gq}, i_{gd}, and i_{gq} are the d-q axis components of the grid voltage and current respectively, u_{gd} and u_{gq} are the d-q axis components of the output voltage of the inverter, and ω is the angular frequency of the grid voltage. In the ultra-local model, F_d and F_q contain the structural information of the known and unknown parts of the system, and α is the input quantity proportional coefficient.

When the grid voltage vector orientation control is adopted, $e_{gq} = 0$, and the active power P_g and reactive power Q_g of the grid side inverter system can be expressed as

$$\begin{cases} P_g = \dfrac{3}{2} e_{gd} i_{gd} \\ Q_g = -\dfrac{3}{2} e_{gd} i_{gq} \end{cases}. \tag{3}$$

According to the power conservation, from Eq. (1) and Eq. (3), the relationship between i_G and i_{gd} is as follows:

$$i_{gd} = \frac{u_{dc} i_G}{1.5 e_{gd}}. \tag{4}$$

3 The proposed SMC-MFPC algorithm

The structural block diagram of the proposed SMC-MFPC algorithm in this paper is shown in Fig. 1. The outer voltage loop regulates the DC link voltage through the SMC algorithm, the inner current loop uses MFPC to achieve precise tracking of the grid-connected current, and a DESO is adopted to estimate the unknown disturbances of the system. This approach ensures the constancy of the DC voltage while enhancing the power quality of grid connection and the disturbance rejection performance.

3.1 SMC controller for DC link voltage

To achieve stable control of the DC link voltage, a sliding mode controller is constructed to address internal and external disturbances of the system. Since the DC link voltage is typically a constant value, the reference voltage u_{ref} is set as a constant, based on which the sliding mode surface is defined:

$$s = u_{ref} - u_{dc}. \tag{5}$$

To optimize the dynamic characteristics of the sliding mode motion, an improved power reaching law with an exponential reaching term is introduced based on [7], and its expression is:

$$\dot{s} = -\varepsilon |s|^{\beta} \operatorname{sgn}(s) - \gamma s \quad (\varepsilon > 0,\ \gamma > 0,\ 0 < \beta < 1). \tag{6}$$

This reaching law integrates the advantages of exponential reaching and power reaching. Compared with the traditional power reaching law, it can suppress sliding mode chattering while ensuring fast state convergence, and provides more flexible adjustment degrees of freedom through ε, γ, and β.

Differentiating the sliding mode surface s, combining with the system current relationship, and substituting Eq. (1) for derivation, it can be obtained that:

$$\dot{s} = -\dot{u}_{dc} = \left(i_G - i_M\right) / C_{dc}. \tag{7}$$

By combining Eqs. (4), (6) and (7), and through the derivation of controller design, the reference command of the grid side d-axis current is finally obtained:

$$i_{gd}^{*} = \frac{2u_{dc}}{3e_{gd}} \left(i_M - C_{dc}\left(\varepsilon |s|^{\beta} \operatorname{sgn}(s) + \gamma s\right)\right). \tag{8}$$

Since i_M is the current output by the MSC, which contains many high-frequency components after rectification, a first-order low-pass filter is used to smooth the measured signal when collecting its signal. The transfer function of the first-order low-pass filter is shown in Eq. (9):

$$H(s) = \frac{1}{s/\omega_c + 1}. \tag{9}$$

Where ω_c is the cutoff angular frequency, and its magnitude should be reasonably selected. If it is too small, the response will be slow and there will be a delay; if it is too large, the filtering effect will be poor.

The quadratic function of the sliding mode surface s is selected as the Lyapunov function:

$$V = s^2 / 2. \tag{10}$$

Taking the derivative of Eq. (10) and substituting the proposed reaching law, it can be obtained that:

$$\dot{V} = s\dot{s} = -\varepsilon |s|^{\beta} \operatorname{sgn}(s) s - \gamma s^2 = -\varepsilon |s|^{\beta+1} - \gamma s^2. \tag{11}$$

Due to $\varepsilon > 0$, $\gamma > 0$, it is obvious that:

$$\begin{cases} \dot{V} < 0 & (s \neq 0) \\ \dot{V} = 0 & (s = 0) \end{cases}. \tag{12}$$

It can be concluded that the sliding mode control system is asymptotically stable through Lyapunov's second method.

3.2 Design of DESO

After discretizing Eq. (2) with the sampling period T_s, it can be obtained that:

$$\begin{cases} i_{gd}(k+1) = i_{gd}(k) + T_s\left(\alpha u_{gd}(k) + F_d(k)\right) \\ i_{gq}(k+1) = i_{gq}(k) + T_s\left(\alpha u_{gq}(k) + F_q(k)\right) \end{cases}. \tag{13}$$

To obtain the values of F_d and F_q in the ultra-local model, this paper designs the DESO for the *d*-axis, and the process for the *q*-axis is similar.

The comprehensive term F_d of the system structure and disturbances changes slowly, and when the sampling time is small, it can be expressed as

$$F_d(k+1) = F_d(k). \tag{14}$$

Based on Eqs. (13) and (14), the DESO is constructed as follows:

$$\begin{cases} \hat{i}_{gd}(k+1) = \hat{i}_{gd}(k) + T_s\left(\alpha u_{gd}(k) + \hat{F}_d(k)\right) \\ +l_1\left(i_{gd}(k) - \hat{i}_{gd}(k)\right) \\ \hat{F}_d(k+1) = \hat{F}_d(k) + l_2\left(i_{gd}(k) - \hat{i}_{gd}(k)\right) \end{cases}. \tag{15}$$

In Eq. (15), l_1 and l_2 are the observer gain coefficients. The observation errors of i_{gd} and F_d are:

$$\begin{cases} \tilde{i}_{gd}(k) = i_{gd}(k) - \hat{i}_{gd}(k) \\ \tilde{F}_d(k) = F_d(k) - \hat{F}_d(k) \end{cases}. \tag{16}$$

Substituting Eqs. (13) and (15) into Eq. (16) yields the matrix form of the error equation:

$$\begin{bmatrix} \tilde{x}_{gd}(k+1) \\ \tilde{F}_d(k+1) \end{bmatrix} = \underbrace{\begin{bmatrix} 1-l_1 & T_s \\ -l_2 & 1 \end{bmatrix}}_{\boldsymbol{A}_{\mathrm{ESO}}} \begin{bmatrix} \tilde{x}_{gd}(k) \\ \tilde{F}_d(k) \end{bmatrix}. \tag{17}$$

When the modulus of all eigenvalues of the state transition matrix $\boldsymbol{A}_{\mathrm{ESO}}$ of the error equation is less than 1, the observer is stable. For the selection of the magnitudes of l_1 and l_2, the pole placement method is used in this paper:

$$\eta^2 - (2 - l_1)\eta + (1 - l_1 + T_s l_2) = \eta^2 - (\eta_1 + \eta_2)\eta + \eta_1\eta_2. \tag{18}$$

When the modulus of the eigenvalues is close to 0, the observer responds quickly but is susceptible to noise; when it is close to 1, the observer has strong noise resistance but slow response. Therefore, this paper designs the eigenvalues to be 0.6.

3.3 MFPC controller for grid-side current

MFPC relies on two core elements: the prediction time domain and the control time domain. The prediction time domain covers the interval from the current moment to a certain future moment, with a length that is an integer multiple of the MFPC sampling time ($N_p \times T_s$), which is used to define the prediction range of state variables; similarly, the control time domain is defined by an integer multiple of the sampling time ($N_c \times T_s$) to clarify the calculation interval of optimal control variables, and $N_c \leq N_p$. By establishing a discretized model of the system and predicting future states, model predictive control can quickly respond to system disturbances and achieve precise control of power.

The observed quantities $\hat{F}_d$ and $\hat{F}_q$ obtained through DESO replace F_d and F_q in Eq. (13), and are written in the form of a matrix equation:

$$\begin{cases} \boldsymbol{i}_g(k+1) = \boldsymbol{A}\boldsymbol{i}_g(k) + \boldsymbol{B}\boldsymbol{u}(k) + \boldsymbol{d}(k) \\ \boldsymbol{i}_g(k) = \left[i_{gd}(k) \quad i_{gq}(k)\right]^{\top} \\ \boldsymbol{u}(k) = \left[u_{gd}(k) \quad u_{gq}(k)\right]^{\top} \\ \boldsymbol{d}(k) = \left[T_s\hat{F}_d(k) \quad T_s\hat{F}_q(k)\right]^{\top} \\ \boldsymbol{A} = \begin{bmatrix} 1 & 0 \\ 0 & 1 \end{bmatrix}, \quad \boldsymbol{B} = \begin{bmatrix} T_s\alpha & 0 \\ 0 & T_s\alpha \end{bmatrix} \end{cases}. \tag{19}$$

In this paper, the control time domain step size N_c is selected as 1. It is assumed that the comprehensive terms F_d and F_q change slowly and can be considered to remain constant within a prediction horizon. Then, the prediction model of the system is:

$$\begin{cases} \boldsymbol{i}_g(k+1) = \boldsymbol{A}\boldsymbol{i}_g(k) + \boldsymbol{B}\boldsymbol{u}(k) + \boldsymbol{d}(k) \\ \boldsymbol{i}_g(k+2) = \boldsymbol{A}^2\boldsymbol{i}_g(k) + (\boldsymbol{A}\boldsymbol{B} + \boldsymbol{B})\boldsymbol{u}(k) + (\boldsymbol{A} + \boldsymbol{E}_2)\boldsymbol{d}(k) \\ \cdots \\ \boldsymbol{i}_g(k+N_p) = \boldsymbol{A}^2\boldsymbol{i}_g(k) + \sum_{i=0}^{N_p-1}\boldsymbol{A}^i\boldsymbol{B}\boldsymbol{u}(k) + \sum_{i=0}^{N_p-1}\boldsymbol{A}^i\boldsymbol{d}(k) \end{cases} \tag{20}$$

where $\boldsymbol{E}_2$ is the 2nd-order identity matrix.

Rewrite Eq. (20) in a more compact form:

$$\begin{cases} \boldsymbol{I}_g[k]=\boldsymbol{\Phi}\boldsymbol{i}_g(k)+\boldsymbol{\Gamma}\boldsymbol{u}(k)+\boldsymbol{D} \\ \boldsymbol{I}_g[k]=\left[\boldsymbol{i}_g(k+1) \quad \boldsymbol{i}_g(k+2) \quad \cdots \quad \boldsymbol{i}_g(k+N_p)\right]^{\top} \\ \boldsymbol{\Phi}=\left[\boldsymbol{A} \quad \boldsymbol{A}^2 \quad \cdots \quad \boldsymbol{A}^{N_p}\right]^{\top} \\ \boldsymbol{\Gamma}=\left[\boldsymbol{B} \quad \boldsymbol{AB}+\boldsymbol{B} \quad \cdots \quad \sum_{i=0}^{N_p-1}\boldsymbol{A}^i\boldsymbol{B}\right]^{\top} \\ \boldsymbol{D}=\left[\boldsymbol{d}(k) \quad (\boldsymbol{A}+\boldsymbol{E}_2)\boldsymbol{d}(k) \quad \cdots \quad \sum_{i=0}^{N_p-1}\boldsymbol{A}^i\boldsymbol{d}(k)\right]^{\top} \end{cases}. \tag{21}$$

To ensure that the reference trajectory can smoothly and gradually guide the system output toward the target value, balance the tracking speed and stability, and reduce overshoot and fluctuations, a first-order exponential reference trajectory is adopted:

$$\boldsymbol{i}_{ref}(k+i)=\boldsymbol{i}_g^*(k)-\mathrm{e}^{-iT_s/\tau}\left[\boldsymbol{i}_g^*(k)-\boldsymbol{i}_g(k)\right] \tag{22}$$

where $\boldsymbol{i}_g^*(k)=\left[i_{gd}^*(k) \quad i_{gq}^*(k)\right]^{\top}$ is the reference of dq-axis current, and $i = 1, 2, \ldots, N_p$.

Thus, the reference trajectory vector can be written as

$$\boldsymbol{I}_{ref}[k]=\left[\boldsymbol{i}_{ref}(k+1) \quad \boldsymbol{i}_{ref}(k+2) \quad \cdots \quad \boldsymbol{i}_{ref}(k+N_p)\right]^{\top}. \tag{23}$$

To obtain the optimal control quantity that minimizes the gap between the reference value and the predicted output, and considering the limit of the actual control voltage, a constrained cost function is defined as

$$\begin{cases} \min J(\boldsymbol{u}(k))=\left\|\boldsymbol{I}_g[k]-\boldsymbol{I}_{ref}[k]\right\|_{\boldsymbol{Q}}^2+\left\|\boldsymbol{u}(k)\right\|_{\boldsymbol{R}}^2 \\ =\left\|\boldsymbol{\Phi}\boldsymbol{i}_g(k)+\boldsymbol{\Gamma}\boldsymbol{u}(k)+\boldsymbol{D}-\boldsymbol{I}_{ref}[k]\right\|_{\boldsymbol{Q}}^2+\left\|\boldsymbol{u}(k)\right\|_{\boldsymbol{R}}^2 \\ \text{s.t.} \quad \left\|\boldsymbol{u}(k)\right\|_2^2 \le u_{\max}^2 \end{cases}. \tag{24}$$

In Eq. (24) $\boldsymbol{Q}$ is the state weight matrix, which is used to allocate priorities for the accuracy of tracking reference values of different state variables; $\boldsymbol{R}$ is the control weight matrix, which is used to limit the amplitude of control inputs.

$$\begin{cases} \boldsymbol{Q}=\mathrm{diag}\left(q_1,q_2,\cdots,q_{2N_p}\right) & \left(q_1,q_2,\cdots,q_{2N_p}>0\right) \\ \boldsymbol{R}=\mathrm{diag}\left(r_1,r_2\right) & \left(r_1,r_2>0\right) \end{cases} \tag{25}$$

Thus, Eq. (24) is a convex optimization problem, and the optimal control quantity is solved by the KKT (Karush-Kuhn-Tucker) conditions. The Lagrangian function is defined as

$$L(\boldsymbol{u}(k),\lambda)=J(\boldsymbol{u}(k))+\lambda\left(\left\|\boldsymbol{u}(k)\right\|_2^2-u_{\max}^2\right). \tag{26}$$

In Eq. (26), λ denotes the Lagrange multiplier, and the KKT conditions are:

$$\begin{cases} \dfrac{\partial L}{\partial \boldsymbol{u}(k)}=\boldsymbol{0} \\ \left\|\boldsymbol{u}(k)\right\|_2^2-u_{\max}^2\le 0 \\ u_{\max}=\dfrac{u_{ref}}{\sqrt{3}} \\ \lambda\ge 0 \\ \lambda\left(\left\|\boldsymbol{u}(k)\right\|_2^2-u_{\max}^2\right)=0 \end{cases}. \tag{27}$$

By combining the equations in Eqs. (26) and (27), the optimal control quantity $\boldsymbol{u}^*(k)$ can be solved as follows: First, set $\lambda = 0$. If $\boldsymbol{u}(k)$ satisfies the constraint conditions in Eq. (24), it is the desired optimal control quantity at this moment.

$$\begin{cases} \boldsymbol{u}(k)=-\boldsymbol{H}^{-1}\boldsymbol{f} \\ \boldsymbol{H}=\boldsymbol{\Gamma}^{\top}\boldsymbol{Q}\boldsymbol{\Gamma}+\boldsymbol{R} \\ \boldsymbol{f}=\boldsymbol{\Gamma}^{\top}\boldsymbol{Q}\left(\boldsymbol{\Phi}\boldsymbol{i}_g(k)+\boldsymbol{D}-\boldsymbol{I}_{ref}\right) \end{cases} \tag{28}$$

If $\boldsymbol{u}(k)$ does not satisfy the constraint conditions in Eq. (24), the constraint is activated, and at this time $\lambda > 0$, then the optimal control quantity is:

$$\boldsymbol{u}(\lambda)=-\left(\boldsymbol{H}+\lambda\boldsymbol{E}_2\right)^{-1}\boldsymbol{f}. \tag{29}$$

Since λ is unknown, it needs to be solved by Newton's method. The steps are as follows:

- Substitute $\boldsymbol{u}(\lambda)$ into the constraint $\left\|\boldsymbol{u}(\lambda)\right\|_2^2=u_{\max}^2$ and construct the objective function:

$$g(\lambda)=\left\|-\left(\boldsymbol{H}+\lambda\boldsymbol{E}_2\right)^{-1}\boldsymbol{f}\right\|_2^2-u_{\max}^2=0. \tag{30}$$

- By solving λ through Newton's method iteration, the process stops when the difference between λ_j and λ_{j+1} is sufficiently small. And the iteration formula is:

$$\lambda_{j+1}=\lambda_j-\frac{g(\lambda_j)}{g'(\lambda_j)}, \tag{31}$$

where the derivative of the objective function is:

$$g'(\lambda)=-2\boldsymbol{f}^{\top}\left(\boldsymbol{H}+\lambda\boldsymbol{E}_2\right)^{-3}\boldsymbol{f}. \tag{32}$$

The purpose of the constraint conditions in Eq. (24) is to enable MFPC to jointly constrain the grid-side current components u_{gd} and u_{gq}. In contrast, traditional PI control can only limit the amplitude of a single control variable, failing to achieve optimal control. If the amplitude of the control voltage vector of the grid-side converter, namely $u_{gdq}=\left\|\boldsymbol{u}(k)\right\|_2$, exceeds its rated amplitude $u_{\max}$, current

prediction errors may occur due to voltage differences, damaging the current tracking performance.

4 Simulation results and analysis

To validate the effectiveness and advantages of the control algorithm proposed in this paper and clarify the impact of different control strategies on system performance, this paper designs multiple sets of comparative simulation experiments, and the MSC and GSC adopt unity power factor control. For the hierarchical control structure of "voltage outer loop - current inner loop" on the grid side of the wind power system, cross-algorithm collaborative comparison is carried out: When comparing the grid-side *d*-*q* axis currents, power, and control quantities, SMC is uniformly adopted for the voltage outer loop, and the inner loop regulation effects of PI, MPC, and MFPC are compared. When comparing the DC link voltage, the MFPC is uniformly used for the current inner loop, and comparisons are made between the outer loop voltage control characteristics of PI and SMC. To ensure the fairness of the comparison, the core parameters of each control algorithm are determined after repeated debugging, and the specific values are shown in Table 1. Additionally, the prediction time domain step size N_p is selected as 3.

The main parameters of the system simulation model are: the blade radius of a 2 MW wind turbine is 35.8 m, the pitch angle is 0°, the moment of inertia is 15000 kg·m^2, and the MPC algorithm is uniformly adopted for the MSC during the simulation. The DC link capacitor is 5 mF, the nominal value of the filter inductor L is 0.6 mH, the filter resistance R_g is 2 mΩ, the rated value of the grid line voltage is 690 V, the grid frequency is 50 Hz, the sampling time T_s is 0.1 ms, the cutoff angular frequency ω_c of the low-pass filter is 50 rad/s, the q-axis reference current is 0 A, and the reference voltage u_{ref} is 2000 V.

4.1 External disturbances

Wind speed variation and grid voltage sag faults are considered as external disturbances to the wind power system. The initial wind speed is 8 m/s, which gradually increases to 12 m/s at 0.3 s, and then gradually decreases to 11 m/s at 0.8 s. The grid voltage sags to 80% of the original value at 1 s and recovers at 1.2 s. The specific time-varying conditions are shown in Fig. 2.

Table 1 Controller parameters

Control Loop	PI	SMC	MPC & MFPC
Grid-side *d*-*q* axis currents	Proportional gain: 5 Integral gain: 60		q_1–q_6: 1 r_1–r_2: 1×10^{-6} τ: 1×10^{-5}
DC link voltage	Proportional gain: 2 Integral gain: 60	ε: 500 β: 0.7 γ: 300	

Under the conditions of wind speed and voltage changes, the simulation curve of i_{gd} is shown in Fig. 3.

As can be observed from Fig. 3, all three current control methods are capable of achieving steady state regulation of i_{gd} under the action of external disturbances. However, it can be seen from the local enlarged view that during the grid voltage sag period, the amplitude of the current ripple under the PI control strategy is the largest. The MPC control strategy has the optimal current smoothness and steady state performance, while the control effect of MFPC lies between the two methods. It should be pointed out that although there are obvious differences in current ripple among different control methods during the transient period, due to the large moment of inertia of the wind turbine generator set itself and the fact that the output active power will be adjusted by the controller on the generator side, finally, the steady state *d*-axis currents of the three control algorithms after external disturbances can all converge to a similar level.

Under the condition of external disturbances, the simulation curve of i_{gq} is shown in Fig. 4.

It can be observed from Fig. 4 that, since external disturbances affect the active power and the *d*-axis current

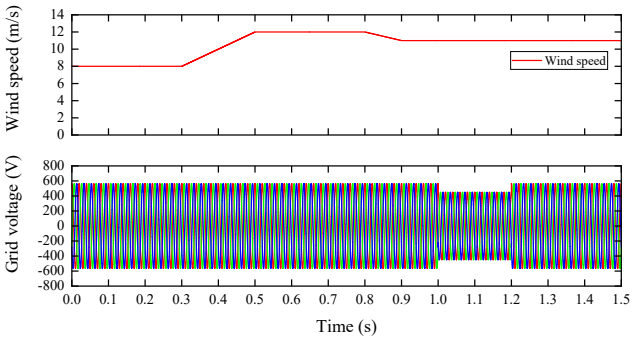

Fig. 2 External disturbances

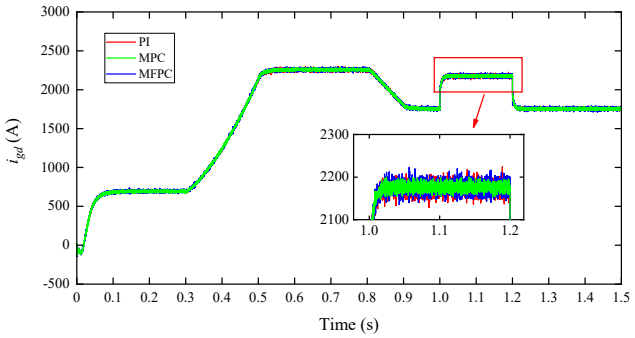

Fig. 3 The *d*-axis current under external disturbances

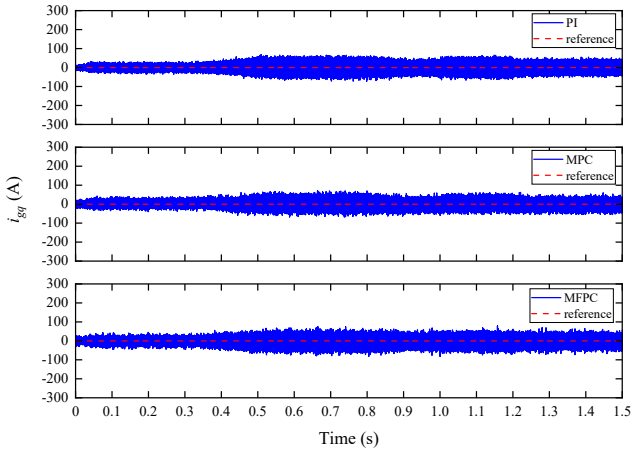

Fig. 4 The *q*-axis current under external disturbances

to a greater extent, the *q*-axis current can stably track the reference value of 0 under all three control algorithms, and the control effects are very similar.

Under the condition of external disturbances, the simulation curves of active power and reactive power output by the system are shown in Fig. 5.

It can be seen from Fig. 5 that the active power and reactive power of the three control methods can be stably input into the power grid under external disturbances, and can quickly adjust and output the power when the grid voltage changes abruptly at 1 s and 1.2 s.

The simulation curve of the voltage vector amplitude of the system control quantity under external disturbances is shown in Fig. 6.

Fig. 6 demonstrates the ability of the three methods to constrain the magnitude of the control variable. It can be seen that the magnitude of the control voltage vector u_{gdq} is restricted below $u_{\max}$ when using the MPC and MFPC methods. In contrast, due to the PI control's ability to only limit the magnitude of a single control variable, u_{gdq} exceeds $u_{\max}$ at some moments. Meanwhile, the ripple situation of the *dq*-axis current under the three algorithms can also be indirectly inferred from the curve of u_{gdq}.

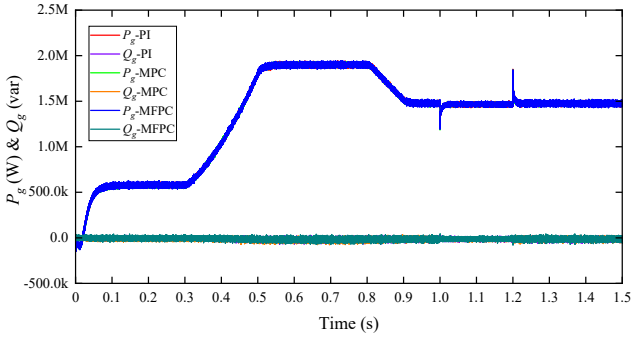

Fig. 5 The power under external disturbances

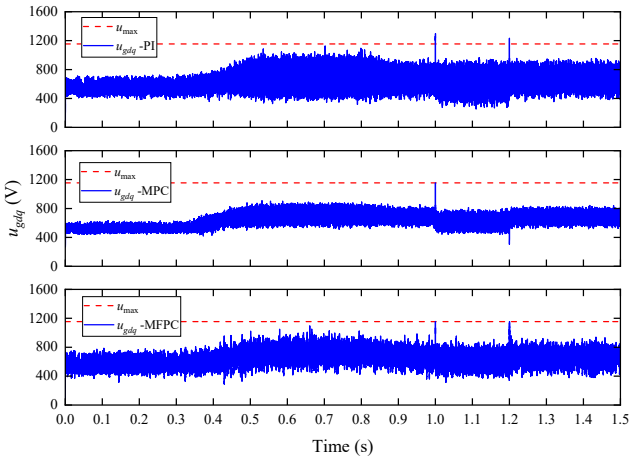

Fig. 6 The amplitude of the control voltage vector under external disturbances

When subjected to external disturbances, the DC link voltage curves under PI control and sliding mode control are shown in Fig. 7.

As is clearly illustrated in Fig. 7, the DC link voltage regulated by the PI control strategy exhibits a more significant overshoot and a longer settling time in comparison to that under the SMC scheme. Specifically, the maximum voltage fluctuation of the PI-controlled system reaches 181 V, whereas the counterpart for the SMC-based system is merely 69 V, highlighting the superior dynamic performance of the latter in suppressing DC link voltage deviations.

4.2 Internal disturbances

During the simulation, the actual value of the filter inductor is changed to verify the ability of the proposed MFPC to resist parameter variations. The filter inductor abruptly changes from 0.6 mH to 0.3 mH at 0.5 s, and then abruptly changes to 1.2 mH at 1 s. The wind speed is maintained at 12 m/s, and the grid line voltage is maintained at 690 V.

Under the condition of inductance parameter perturbation, the simulation curve of i_{gd} is shown in Fig. 8.

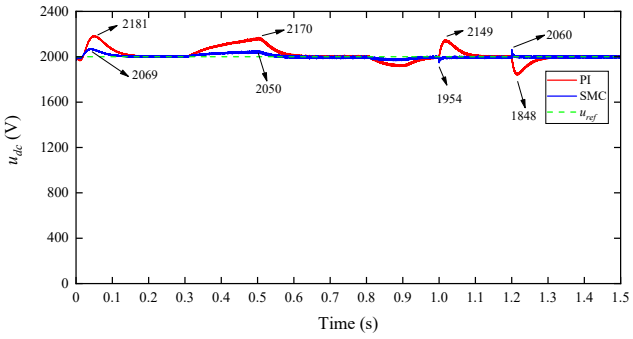

Fig. 7 DC link voltage under external disturbances

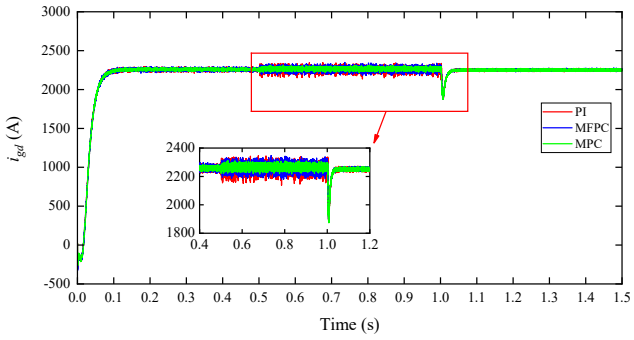

Fig. 8 The *d*-axis current under internal disturbances

It can be seen from Fig. 8 that the three current control methods all achieve stable control of i_{gd} when the internal inductance changes. From the partial enlarged view, it can be observed that during the period when the inductance is reduced to half of the nominal value, the current ripple under PI control is the largest; MPC control has the best steady state performance, and the current ripple of MFPC is slightly smaller than that of PI.

The simulation curve of i_{gq} is shown in Fig. 9. As can be seen from Fig. 9, when the inductance parameter undergoes abrupt changes, the three control methods exhibit significant differences in their performance in regulating the *q*-axis current. At 0.5 s, the inductance value suddenly drops to 50% of the nominal value. At this point, the current ripple under the PI control strategy is the largest; the average current under MPC control has deviated from the reference value by approximately 100 A; whereas the MFPC control can achieve stable tracking of the 0 A reference value. At 1 s, the inductance value suddenly increases to 200% of the nominal value. Among them, the current under PI control stabilizes at 0 A after 0.2 s of adjustment; the MPC control can no longer achieve zero-error tracking of the reference value, showing an obvious steady state

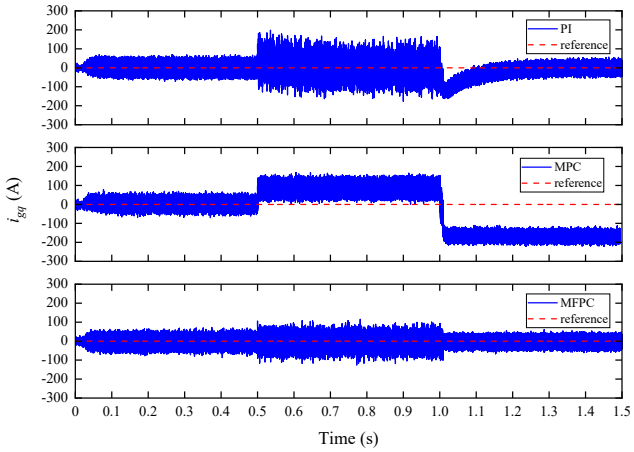

Fig. 9 The *q*-axis current under internal disturbances

error with an amplitude of about 150 A; in contrast, due to the adoption of an ultra-local model that can be corrected in real time, the MFPC control maintains an accurate tracking effect with nearly zero adjustment time and zero error throughout the process.

The simulation curves of active power and reactive power output by the system under the condition of filter inductance parameter changes are shown in Fig. 10.

It can be observed from Fig. 10 that due to the change of inductance, although the active power of the three control methods can be effectively output, only MFPC always maintains the reactive power at 0 var. PI has an adjustment time, and MPC can no longer maintain the output of 0 var.

The simulation curve of the voltage vector amplitude of the system control quantity under internal disturbances is shown in Fig. 11.

As can be seen from Fig. 11, the PI control is no longer able to effectively limit the amplitude of the control voltage vector at this point, while the excellent constraint handling capabilities of MPC and MFPC are demonstrated. The magnitude of the *dq*-axis current ripples under the three algorithms is also indirectly verified through the curves of u_{gdq}.

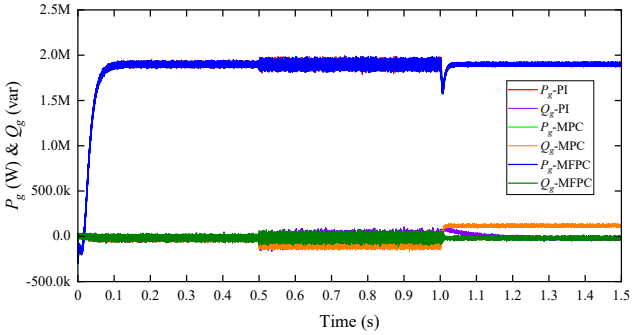

Fig. 10 The power under internal disturbances

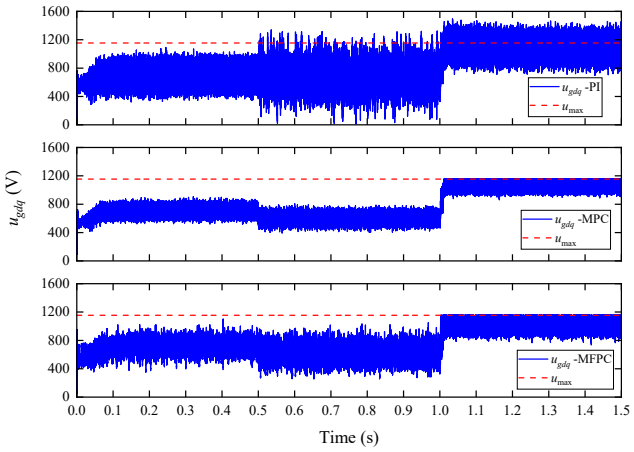

Fig. 11 The amplitude of the control voltage vector under internal disturbances

When subjected to internal disturbances, the DC link voltage curves under PI control and sliding mode control are shown in Fig. 12.

It can be observed that under system internal disturbances, the SMC still exhibits significantly superior performance to the PI control in terms of DC link voltage control. Specifically, when the filter inductance parameter abruptly changes from 0.3 mH to 1.2 mH at 1 s, the maximum voltage fluctuation amplitude under PI control reaches 150 V, while that under SMC control is only 93 V. This fully demonstrates the stronger dynamic regulation capability of SMC.

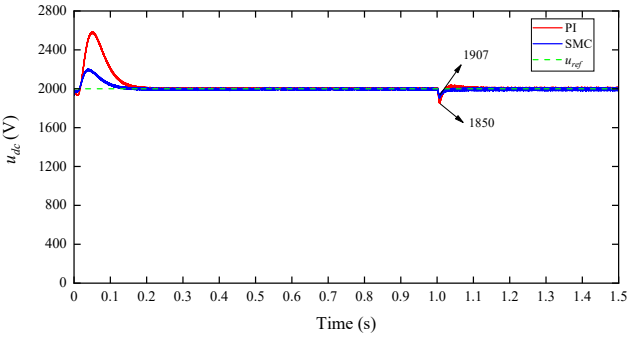

Fig. 12 DC link voltage under internal disturbances

5 Conclusion

This paper proposes an SMC-MFPC control algorithm for the grid-side control of direct-drive wind turbines, which can achieve the efficient and precise power generation target of the wind power generation system under internal and external disturbances. First, an SMC algorithm for the DC link voltage is designed. Then, aiming at the problem of grid-side filter inductance variation, an MFPC control method is proposed, and the comprehensive term of system structure information and disturbances is observed through DESO to avoid the degradation of control performance caused by model inaccuracies. Simulation results show that when wind speed and grid voltage fluctuate, SMC more effectively suppresses DC side voltage fluctuations compared with traditional PI control. When facing changes in inductance values, MFPC demonstrates better control performance than traditional PI and MPC, which helps wind turbines operate efficiently for a long time in harsh internal and external environments.

References

[1] Pan, L., Shao, C. "Wind energy conversion systems analysis of PMSG on offshore wind turbine using improved SMC and Extended State Observer", Renewable Energy, 161, pp. 149–161, 2020. https://doi.org/10.1016/j.renene.2020.06.057

[2] Nguyen, P. T. H., Stüdli, S., Braslavsky, J. H., Middleton, R. H. "Lyapunov stability of grid-connected wind turbines with permanent magnet synchronous generator", European Journal of Control, 65, 100615, 2022. https://doi.org/10.1016/j.ejcon.2022.100615

[3] Wu, J., Li, J., Wang, H., Li, G., Ru, Y. "Fault-Tolerant Three-Vector Model-Predictive-Control-Based Grid-Connected Control Strategy for Offshore Wind Farms", Electronics, 13(12), 2316, 2024. https://doi.org/10.3390/electronics13122316

[4] He, Y., Tang, Y., Gao, X., Xie, H., Wang, F., Rodriguez, J., Kennel, R. "Direct Predictive Voltage Control for Grid-Connected Permanent Magnet Synchronous Generator System", IEEE Transactions on Industrial Electronics, 70(11), pp. 10860–10870, 2023. https://doi.org/10.1109/TIE.2022.3227277

[5] Yassin, H. M., Hanafy, H. H., Hallouda, M. M. "Enhancement low-voltage ride through capability of permanent magnet synchronous generator-based wind turbines using interval type-2 fuzzy control", IET Renewable Power Generation, 10(3), pp. 339–348, 2016. https://doi.org/10.1049/iet-rpg.2014.0453

[6] Errami, Y., Ouassaid, M., Maaroufi, M. "A performance comparison of a nonlinear and a linear control for grid connected PMSG wind energy conversion system", International Journal of Electrical Power & Energy Systems, 68, pp. 180–194, 2015. https://doi.org/10.1016/j.ijepes.2014.12.027

[7] Osman, A. M., Alsokhiry, F. "Sliding Mode Control for Grid Integration of Wind Power System Based on Direct Drive PMSG", IEEE Access, 10, pp. 26567–26579, 2022. https://doi.org/10.1109/ACCESS.2022.3157311

[8] Prince, M. K. K., Arif, M. T., Haque, M. E., Gargoom, A., Oo, A. M. T. "Design and implementation of finite control set MPC with an *LCL* filter for grid-tied PMSG based wind turbine", International Journal of Electrical Power & Energy Systems, 152, 109197, 2023. https://doi.org/10.1016/j.ijepes.2023.109197

[9] Ma, X., Yu, J., Yang, P., Wang, P., Zhang, P. "An MPC based active and reactive power coordinated control strategy of PMSG wind turbines to enhance the support capability", Frontiers in Energy Research, 11, 1159946, 2023. https://doi.org/10.3389/fenrg.2023.1159946

[10] Wei, Y., Ke, D., Yu, X., Wang, F., Rodríguez, J. "Adaptive Inertia Observer-Based Model-Free Predictive Current Control for PMSM Driving System of Electric Vehicles", IEEE Transactions on Industry Applications, 60(4), pp. 6252–6262, 2024. https://doi.org/10.1109/TIA.2024.3396123

[11] Ma, C., Li, H., Yao, X., Zhang, Z., De Belie, F., "An Improved Model-Free Predictive Current Control With Advanced Current Gradient Updating Mechanism", IEEE Transactions on Industrial Electronics, 68(12), pp. 11968–11979, 2021. https://doi.org/10.1109/TIE.2020.3044809

[12] Sun, Z., Deng, Y., Wang, J., Yang, T., Wei, Z., Cao, H. "Finite Control Set Model-Free Predictive Current Control of PMSM With Two Voltage Vectors Based on Ultralocal Model", IEEE Transactions on Power Electronics, 38(1), pp. 776–788, 2023. https://doi.org/10.1109/TPEL.2022.3198990

[13] Yuan, L., Mei, J.-W., Xu, A., Li, X. "Model-Free Predictive Control With Super-Twisting Observer of Single-Phase Neutral-Clamped H-Bridge Cascade Inverters With Fixed Switching Frequency", IEEE Journal of Emerging and Selected Topics in Power Electronics, 13(2), pp. 2410–2421, 2025. https://doi.org/10.1109/JESTPE.2024.3508749

[14] Khalilzadeh, M., Vaez-Zadeh, S., Rodriguez, J., Heydari, R. "Model-Free Predictive Control of Motor Drives and Power Converters: A Review", IEEE Access, 9, pp. 105733–105747, 2021. https://doi.org/10.1109/ACCESS.2021.3098946

[15] Nauman, M., Shireen, W., Hussain, A. "Model-Free Predictive Control and Its Applications", Energies, 15(14), 5131, 2022. https://doi.org/10.3390/en15145131

[16] Zhou, Y., Li, H., Liu, R., Mao, J. "Continuous Voltage Vector Model-Free Predictive Current Control of Surface Mounted Permanent Magnet Synchronous Motor", IEEE Transactions on Energy Conversion, 34(2), pp. 899–908, 2019. https://doi.org/10.1109/TEC.2018.2867218

[17] Feng, Y., Zhang, C., Huang, S., Zhang, S., Qu, J., Li, Z., Zhai, L., Zhao, Y. "An Improved Model-Free Predictive Current Control for PMSM Drives Based on Current Circle Tracking Under Low-Speed Conditions", IEEE Access, 12, pp. 57767–57779, 2024. https://doi.org/10.1109/ACCESS.2024.3388252

[18] Zhang, Y., Jin, J., Huang, L. "Model-Free Predictive Current Control of PMSM Drives Based on Extended State Observer Using Ultralocal Model", IEEE Transactions on Industrial Electronics, 68(2), pp. 993–1003, 2021. https://doi.org/10.1109/TIE.2020.2970660

[19] Babayomi, O., Zhang, Z. "Model-Free Predictive Control of Power Converters with Multifrequency Extended State Observers", IEEE Transactions on Industrial Electronics, 70(11), pp. 11379–11389, 2023. https://doi.org/10.1109/TIE.2022.3225819

[20] Zhang, Z., Ma, J., Qiu, L., Liu, X., Xu, B., Fang, Y. "Extended ISMO-Based Two-Step Prediction Horizon Model-Free Predictive Control for Power Converters", IEEE Journal of Emerging and Selected Topics in Power Electronics, 13(1), pp. 408–417, 2025. https://doi.org/10.1109/JESTPE.2024.3421619